Contents lists available at ScienceDirect

Materials & Design

journal homepage: www.elsevier.com/locate/matdes

Formation of fully equiaxed grain microstructure in additively manufactured AlCoCrFeNiTi$_{0.5}$ high entropy alloy

S. Guan [a], K. Solberg [b], D. Wan [b], F. Berto [b], T. Welo [b], T.M. Yue [a], K.C. Chan [a, *]
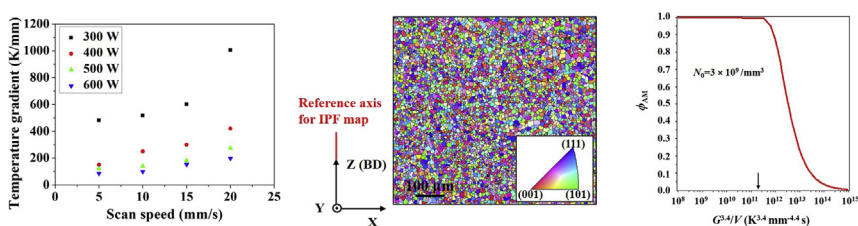
[a] Advanced Manufacturing Technology Research Center, Department of Industrial and Systems Engineering, The Hong Kong Polytechnic University, Hung Hom, Kowloon, Hong Kong
[b] Department of Mechanical and Industrial Engineering, Norwegian University of Science and Technology, Richard Birkelands vei 2B, 7491 Trondheim, Norway

HIGHLIGHTS

- Fully equiaxed grain microstructures are easily achieved in additively manufactured high entropy alloy AlCoCrFeNiTi$_{0.5}$.
- The equiaxed grain formation is attributed to frequent dendrite fragmentation and hence profuse effective nucleation sites.
- A quantitative analysis is performed to provide a theoretical basis for our experimental findings.

GRAPHICAL ABSTRACT

ARTICLE INFO

ABSTRACT

In this work, the non-equiatomic high entropy alloy AlCoCrFeNiTi$_{0.5}$ was additively manufactured via the laser engineered net shaping (LENS™) process. Contrary to the columnar grain microstructure commonly observed in previously reported alloys, the as-deposited AlCoCrFeNiTi$_{0.5}$ specimens exhibit a fully equiaxed grain microstructure in a wide range of temperature gradients G (85 to 1005 K/mm) and solidification velocities V (5 to 20 mm/s). The main microstructural characteristics were found to be B2-structured proeutectic dendrites delineated by lamellar or rod-like B2/A2 eutectic structures. The formation of this microstructural feature can be discussed with the aid of Scheil's solidification model. The proeutectic B2-structured dendrites were frequently found to be fragmented, which may provide profuse effective nucleation sites, and hence promote equiaxed grain formation. Furthermore, we estimated the volume fraction ϕ values of equiaxed crystals at solidification front for various G - V combinations established in this paper, which can provide a theoretical basis for our experimental findings. The current work provides guidelines for producing fully equiaxed alloys by the additive manufacturing (AM) process.

1. Introduction

High entropy alloys (HEAs) define a new and near-infinite compositional space for materials design, enabling the discovery of more diverse microstructures with improved properties [1–3].

This new class of alloys typically forms a single-phase face-centered-cubic (FCC) [4], body-center-cubic (BCC) [5], or hexagonal-close-packed (HCP) [6] structure. Multiple-phase microstructures are also possible in the form of eutectic structures [7], small-scale precipitates embedded in the matrix [8,9], or dual phases of identical chemical composition [10]. Until now, the vast majority of HEAs were typically processed by casting, possibly followed by post processing, e.g. cold forging and annealing

* Corresponding author.

treatments. However, only simple geometry parts are accessible, and post machining is normally needed. These disadvantages are intrinsically associated with this conventional metallurgical route, and are therefore difficult to eliminate. Furthermore, post processing/machining is impossible for certain ultrahigh-strength HEAs. By contrast, additive manufacturing (AM) produces a physical component layer by layer from a digital design, which increases design freedom and manufacturing flexibility. Complex shaped components can be built in a single step by the AM process without any post machining. Moreover, the AM process is a localized melting and solidification process, in essence, which typically creates a strong temperature gradient and high solidification velocity. Therefore, fine grains, and solidification and dislocation substructures can be achieved in the AM-ed alloys, which may lead to excellent mechanical properties, surpassing those of their counterparts fabricated via conventional metallurgical processes [11]. These advantages are the key drivers for the recently increasing interest in fabrication of HEAs using the AM process.

To date, the predominantly studied AM-ed HEAs are AM-ed Al_x-CoCrFeNi [12−19] and CrMnFeCoNi [20−28] alloys. They were manufactured by various AM processes with different processing parameters. Other work includes AM of $Co_{1.5}CrFeNi_{1.5}Ti_{0.5}Mo_{0.1}$ [29], TiZrNbMoV [30], $Co_{0.5}CrCu_{0.5}FeNi_{1.5}AlTi_{0.4}$ [31] and compositionally graded HEAs, i.e. $AlCo_xCr_{1-x}FeNi$ $(0 \leq x \leq 1)$ [32], $Al_xCrCuFeNi_2$ $(0 < x < 1.5)$ [33] and $AlCrFeMoV_x$ $(0 < x < 1)$ [34]. It is typically reported that these AM-ed HEAs are predominantly characterized by columnar and textured microstructures, see e.g. Refs. [12, 17, 20, 22], despite the fact that equiaxed grains are achievable at specific heights/compositions of the compositionally graded HEAs [32−34]. The predominantly columnar and textured microstructures are not surprising and are consistent with those of AM-ed conventional alloys [35−43]. It is widely acknowledged that, for a specific alloy, the temperature gradient G and solidification velocity V concurrently determine the volume fraction ϕ of the equiaxed crystals at solidification front, and hence concurrently control the solidification microstructure during the AM process (i.e. $\phi > 49\%$, fully equiaxed; $\phi < 0.66\%$, fully columnar; $0.66\% < \phi < 49\%$, mixed). Such effects can be quantitatively described by Gäumann's model [44], which takes into accounts high velocity effects and is hence applicable to rapid solidification, e.g. the AM process. In most cases, the G - V combinations (high G, low V) associated with the AM process lead to a ϕ value far below 49% and even below 0.66%, indicating that columnar grain microstructures, typically with crystallographic textures, are formed. Such morphological and crystallographic textures may result in mechanical anisotropy [35,45], which reduces the freedom in component design.

Our work reports a AM-ed fully equiaxed and randomly textured HEA $AlCoCrFeNiTi_{0.5}$, a prototype HEA with multiple-phase microstructures (i.e. disordered A2-structured precipitates embedded in ordered B2-structured matrix) and excellent wear resistance [46−48]. A large density of nucleation sites is estimated from the final solidification microstructure, and microstructural features provide insights into the origin of these nucleation sites. Furthermore, the volume fraction ϕ values of equiaxed crystals at solidification front for various G - V combinations established in this paper are evaluated, with the aid of Gäumann's model [44], to provide a theoretical basis for our experimental findings. The current work provides guidelines to produce fully equiaxed and randomly textured alloys by the AM process.

2. Experimental procedure

2.1. Specimens fabrication via the laser engineered net shaping (LENS™) process

The LENS™ process, a typical laser powder-blown AM process, was used in this study to deposit the $AlCoCrFeNiTi_{0.5}$ alloy. This process typically blows powdered materials, with the aid of argon gas, into a melt pool which is created by a high powered laser beam. The $AlCoCrFeNiTi_{0.5}$ powders used in this study were prepared by inert gas atomization, with nominal chemical composition 18.2%Al, 18.2%Co, 18.2%Cr, 18.2%Fe, 18.2%Ni and 9.1%Ti (at%). Fig. 1 (a) is a SEM micrograph of the $AlCoCrFeNiTi_{0.5}$ powders, which are perfectly spherical. The satellite powders were occasionally observed, and their formations are attributed to the welding of smaller particles to the larger ones during the flight collision [49]. The particle size distributions were measured from SEM images using Nano Measurer software, and are shown in Fig. 1 (b). Such powders are suitable for using in the LENS™ system.

A series of $AlCoCrFeNiTi_{0.5}$ cuboid specimens (8 mm by 8 mm by 6 mm) were manufactured from the above-mentioned powders using different laser powers and laser scan speeds (300−600 W and 5−20 mm/s, respectively). A bidirectional scan path with a hatch spacing of 460 μm, and a cross-hatched scan (i.e. a 90° rotation of the laser scan direction when depositing the subsequent layer) were adopted during the manufacturing process, as shown in Fig. 1 (c). To minimize any potential oxidation, the whole manufacturing process was performed in an enclosed processing chamber with
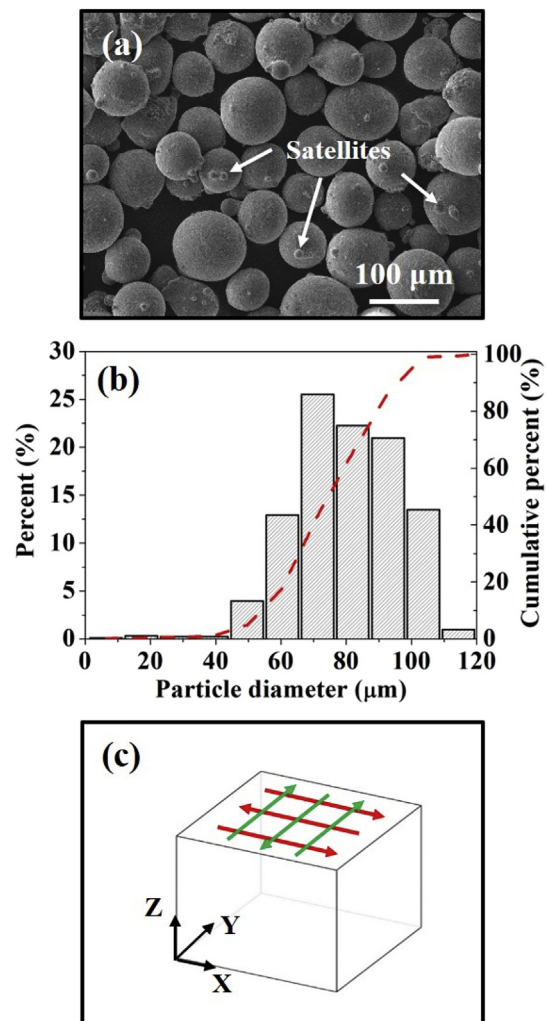

Fig. 1. (a) SEM image showing the $AlCoCrFeNiTi_{0.5}$ powders, with satellite powders indicated by white arrows. (b) Volume-weighted powder size distribution map. (c) Schematic illustration of the cuboid specimen fabricated by the LENS™ process. The red and green arrows represent the laser scan direction for successive two layers, showing the bi-directional and cross-hatched scan strategy. The Z axis indicates the building direction (BD).

<20 ppm oxygen content. To meet the required oxygen level, argon gas was used to purge the processing chamber, until reaching 200 ppm oxygen level. Then the processing chamber was connected to a blower, which drew the argon gas out of the chamber and passed it over the oxygen and moisture getter. The getter absorbed the O_2 and H_2O, and then returned the clean argon to the chamber, and after reaching the required oxygen level (i.e. below 20 ppm), the specimens were manufactured.

During the whole LENS™ process, we monitored the melt pool with the aid of a two-wavelength imaging pyrometer. This imaging pyrometer provides a high resolution (12.1 μm/pixel) and real-time (25 frames/s) temperature measurement, ranging from 1273 to 3073 K. A high temperature tungsten filament was used to calibrate this imaging pyrometer before usage. The temperature data enable us to evaluate the G value during the LENS™ processing.

2.2. Material characterization and thermodynamic calculations

The phase identification was performed on a Rigaku SmartLab X-ray diffractometer with Cu Kα radiation. The scan speed and scan range were 5°/min and 30° ~ 100°, respectively. The microstructural analysis was performed with the aid of scanning electron microscopy (SEM), electron backscatter diffraction (EBSD), and energy dispersive X-ray (EDS) techniques. For SEM, both backscattered electron (BSE) imaging and secondary electron (SE) imaging were used. SEM, EBSD, and EDS investigations were performed at an acceleration voltage of 20 kV. The surface for microstructural analysis (i.e. SEM, EDS, and EBSD) was ground up to 4000 grit size emery paper and polished down to 0.05 μm particle diameter colloidal silica-based slurry.

The thermodynamic calculations were conducted by the CALPHAD (CALculation of PHAse Diagram) method, on the platform of the Thermo-Calc software 2019a equipped with a HEA database. This HEA thermodynamic database enables the calculation of the equilibrium state and Scheil's solidification of HEA systems.

3. Results

3.1. Evaluation of G and V values

Fig. 2 (a) shows a representative color-coded temperature image of the melt pool surface for the AlCoCrFeNiTi$_{0.5}$ alloy deposited at a laser power of 400 W and a scan speed of 5 mm/s. The white arrow represents the laser scan direction. It can be observed from the thermal image that the peak temperature region is approximately located in the melt pool center. The temperature profile was evaluated along the white dashed line in Fig. 2 (a), which passes the peak temperature in the melt pool and is in the laser scan direction, and is shown in Fig. 2 (b). The broken black line indicates the liquidus temperature $T_L = 1620$ K (calculated by Thermo-Calc software) of the AlCoCrFeNiTi$_{0.5}$ alloy. The zero value on the X axis indicates the peak temperature point, which divides the melt pool into heating and cooling regions. Obviously, the latter region needs to be paid more attention. The G value in the cooling region was calculated accordingly, and its profile is shown in Fig. 2 (c). It can be seen that the G value is not a constant in the melt pool, and in this paper we adopt the G value at the melt pool boundary, at which solidification occurs. The melt pool boundary is represented by the crossover point between the temperature curve and the horizontal liquidus temperature line. As shown in Fig. 2 (c), the G value was estimated to be approximately 150 K/mm.

The same method was also used to evaluate the G values corresponding to various laser scan speeds and laser powers used in this study, and the results are summarized in Fig. 2 (d). It can be clearly seen that increase in laser scan speed or decrease in laser power contributes to a larger G value, i.e. a stronger temperature gradient. In summary, the manipulation of the laser scan speeds and laser powers creates a wide range of G values (i.e. 85 to 1005 K/mm). As for the V value at the trailing edge of the melt pool, it is approximately equal to the advance rate of the liquidus isotherm, i.e. the laser scan speed, which is in the range of 5−20 mm/s.

3.2. Equiaxed grain microstructure

Fig. 3 (a) gives the inverse pole figure (IPF) image of an area of 700 μm by 700 μm taken in the XZ-plane of the LENS™-processed AlCoCrFeNiTi$_{0.5}$ specimen deposited at a laser power of 400 W and a laser scan speed of 5 mm/s. Each individual grain in the IPF image was color-coded according to the relationship between its crystallographic orientation and the building direction (BD), which was aligned vertically upwards. Obviously, there is no preferred crystallographic texture developed in the specimen because the grains were randomly color coded. Furthermore, it is interesting to note, from the IPF image, that the grains show perfect equiaxed morphologies in the XZ-plane. To fully reveal the grain microstructure in 3D space, the XZ-, YZ- and XY-planes were characterized by BSE imaging, and the results are shown in Fig. 3 (b). It can be clearly seen that the grains exhibit equiaxed morphologies in all of these three planes, and it is thus confirmed that fully equiaxed grain microstructures in 3D space are formed, rather than columnar grain microstructures which are more common for the AM-ed alloys [35−41]. The statistics show that grains with aspect ratio values larger than 0.3, which can be regarded as equiaxed grains, account for >95.5% of all grains in the scanned area (Fig. 3 (c)). The aspect ratio in the present paper refers to the ratio of the minor axis length to the major axis length of an ellipse fitted to an irregular grain. Moreover, the statistical grain size is Gaussian distributed with a mean value of 12 μm, as shown in Fig. 3 (d). It should be noted that the laser scan speed and laser power (5−20 mm/s, and 300−600 W, respectively) were also varied to deposit the AlCoCrFeNiTi$_{0.5}$ alloy, and a wide range of G and V values have been established (Fig. 2 (d)). However, similar fully equiaxed grain microstructures have been achieved, without any exception, despite a variation in grain size, as shown in Fig. 3 (e)). With the increase of the linear heat input (i.e. the quotient of the laser power and laser scan speed), the cooling rate (i.e. the product of G and V) decreases, which leads to coarser grains. It can be also observed that a critical linear heat input value may exist in this study, beyond which the cooling rate is steady in general and therefore the grain size variation is less pronounced. Anyway, it is confirmed in the present study that fully equiaxed grains dominate the solidification microstructure of the LENS™-deposited AlCoCrFeNiTi$_{0.5}$ alloy. To be more precise, it is the equiaxed solidification, rather than columnar solidification, that dominates the solidification process of the AlCoCrFeNiTi$_{0.5}$ alloy. Furthermore, it should be mentioned that the LENS™-deposited AlCoCrFeNiTi$_{0.5}$ specimens deposited at various laser powers and laser scan speeds show similar phase constitution and microstructure details. Therefore, only one specimen is shown in Sections 3.3 and 3.4. Unless otherwise stated, the specimen shown was deposited at a laser power of 400 W and a laser scan speed of 5 mm/s.

3.3. Phase constitution

Fig. 4 gives the XRD analysis of the LENS™-processed AlCoCrFeNiTi$_{0.5}$ alloy, with the examination surface being the XY-plane. Two BCC phases were detected: one is the ordered BCC-structured (B2) phase, and the other one is the disordered BCC-structured (A2) phase. More specifically, the microstructure of the LENS™-processed AlCoCrFeNiTi$_{0.5}$ specimen consists of B2 and A2 phases, which is consistent with that of the as-casted counterpart [46]. The lattice constants of the B2 and A2 phases were calculated to be $a = 0.2912$ nm and $a = 0.2801$ nm, respectively. Furthermore, it is observed from the inset that the diffraction peaks originating
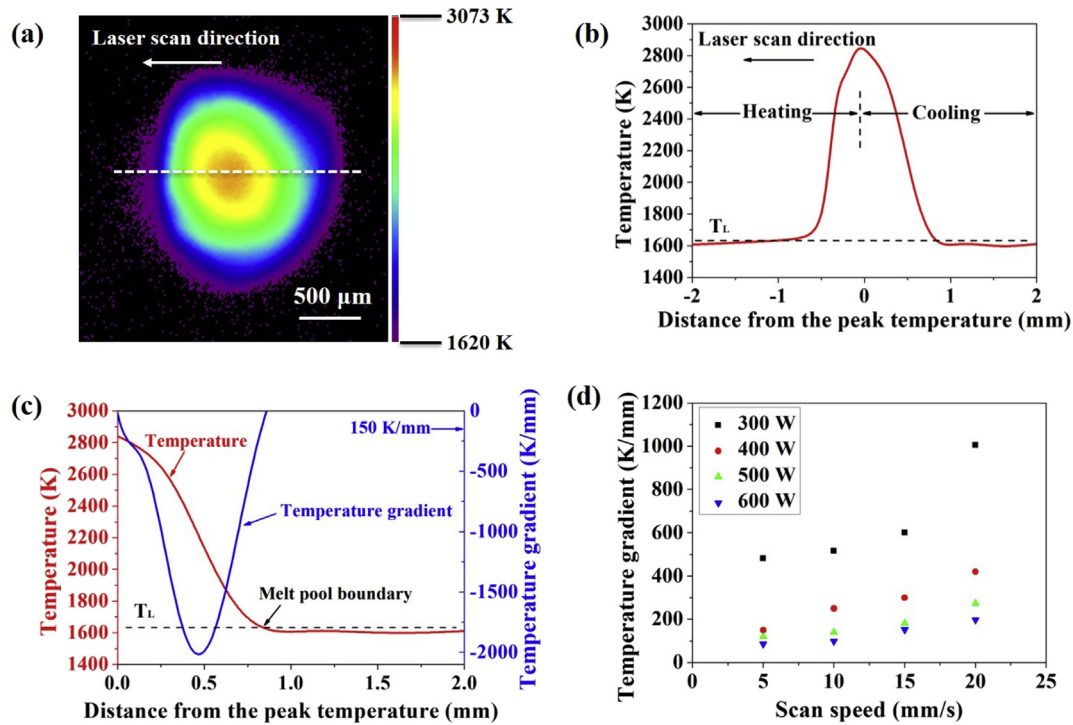
Fig. 2. (a) A representative color-coded temperature image of the melt pool surface for the AlCoCrFeNiTi$_{0.5}$ alloy deposited at a laser power of 400 W and a scan speed of 5 mm/s. The laser scan direction is indicated by a white arrow. (b) Temperature profile along the white dashed line shown in (a), which passes the peak temperature in the melt pool and is in the laser scan direction. The hottest point divides the temperature profile into heating and cooling regions. (c) Temperature profile and corresponding temperature gradient profile in the cooling region. The broken black lines in (b) and (c) indicate the liquidus temperature $T_L = 1620$ K. (d) A summary of temperature gradients corresponding to various laser scan speeds and laser powers.

from the same crystal plane are very close to each other, due to the similar lattice constants of the two phases, in addition to a (100) superlattice peak at $2\theta \approx 30.7°$ originating from B2 phases.

3.4. Microstructural details

Fig. 5 shows the microstructural details of the LENS™-deposited AlCoCrFeNiTi$_{0.5}$ specimen in the SEM BSE imaging mode. It can be clearly seen that the equiaxed grains are delineated by intergranular discrete bright phases (Fig. 5 (a)). Furthermore, the dendritic structure within each equiaxed grain can be seen. BSEs originate from the incident electrons which are back-scattered out of the specimen by specimen atoms. Therefore, phases with heavier elements (i.e. higher atomic number elements) more strongly backscatter electrons and appear brighter, in a BSE image, than phases with lighter elements (i.e. lower atomic number elements). To be more precise, the aforementioned bright phases must contain more heavier elements. Some eutectic structures were also observed, with lamellar or rod morphologies clinging to the edges of proeutectic dendrites (Fig. 5 (b)). Such eutectic structures and proeutectic dendrites belong to a single grain. Furthermore, eutectic cells were also observed at the grain boundaries, rather than adhering to the proeutectic dendrites, and these cells are believed to nucleate and grow independently at the very last stage of solidification. Therefore, these eutectic cells are new grains, which are separated with the adjacent dendrites by grain boundaries. A typical eutectic cell is marked in Fig. 5 (a). Fig. 6 shows the EDS elemental distribution analysis of the AlCoCrFeNiTi$_{0.5}$ alloy. Recalling the phase identification and microstructural details, the bright phases are Cr-Fe-rich A2 phases, and the dark phases are the Ni-Al-Ti-rich B2 phases. Certainly, the eutectic structure is a mixture of B2 and A2 phases. It should be mentioned that in the dark B2 dendrites some bright needle-like precipitates are also formed (Fig. 5 (b)), although they are not detected by EDS due to its resolution limit.

Similar decomposed microstructure is observed in the as-casted counterpart, and is attributed to spinodal decomposition of B2 dendrites into B2 plus A2 coexisting phases (i.e. a solid-state phase transformation process in nature) [47]. The microstructural evolution during solidification is discussed in Section 4.1.

4. Discussion

4.1. Microstructural evolution during solidification

The microstructural evolution during solidification is simulated using Scheil's model on the platform of Thermo-Calc software equipped with a HEA database. It should be noted that Scheil's solidification process is simulated, assuming no diffusion of any elements in the solid but infinite diffusion of all elements in the liquid. Fig. 7 (a) shows the mass fraction of the phases as a function of temperature during solidification. According to this diagram, the solidification mode is L→L+B2→L+B2+A2. More specifically, when the temperature is above 1400 K (and below 1620 K), only the B2 phases solidify from the molten alloy, and the B2- and solid-curves coincide. At this stage, Cr, Fe, and Ti atoms are rejected into the remaining molten alloy, as can be seen in Fig. 7 (b). This means that the first solidified region is enriched in Ni and Al, and the later solidified region is enriched in Cr, Fe, and Ti. At 1400 K, only 12.6% molten alloy is left, and it reaches the eutectic composition. With further decrease of temperature, the B2 and A2 phases are predicted to solidify concurrently, i.e. the eutectic reaction L→B2+A2.

4.2. Equiaxed grain formation mechanism

4.2.1. Density of nucleation sites vs. temperature gradient
The LENS™-deposited AlCoCrFeNiTi$_{0.5}$ alloy exhibits a fully equiaxed grain microstructure at various G - V combinations. This is
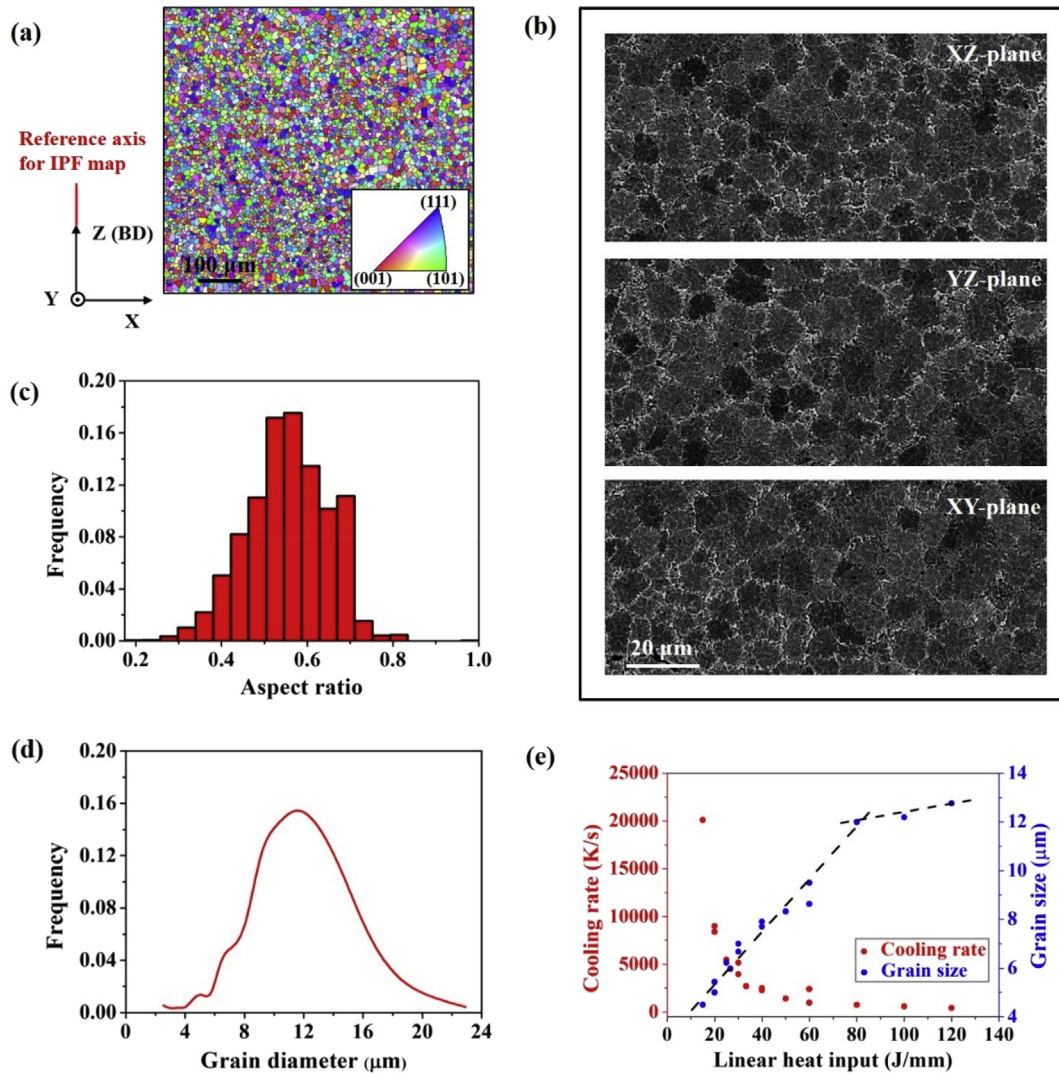
Fig. 3. (a) EBSD-IPF map of the XZ-plane, showing equiaxed grains in this section. (b) BSE images of XZ-, YZ- and XY-planes, confirming fully equiaxed grain microstructures in 3D space. (c) and (d) Statistics of the grain shape aspect ratio and grain size, respectively. (e) Cooling rate and grain size variations with linear heat inputs.
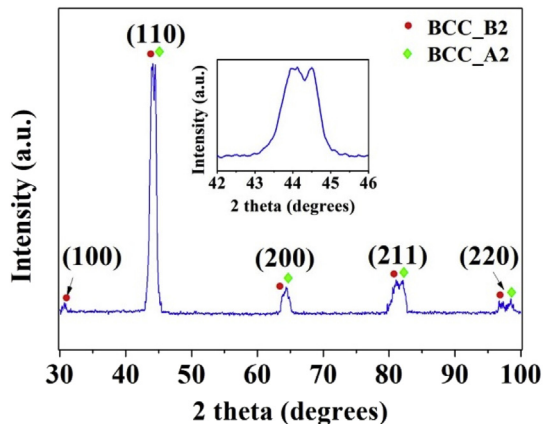

Fig. 4. XRD analysis of the LENS™-processed AlCoCrFeNiTi$_{0.5}$ alloy, with the examination surface being the XY-plane. The co-existence of ordered BCC-structured (B2) and disordered BCC-structured (A2) phases is confirmed. The inset shows an enlarged view of the strongest peak (110).

surprising, and not consistent with commonly reported AM-ed HEAs [12,17,20,22] and AM-ed conventional alloys [35–43]. As mentioned before, the G - V combinations associated with the AM process facilitate columnar solidification, and hence promote the formation of columnar grain microstructures [44]. More specifically, it is the very large G value that is responsible for the columnar solidification during the AM process. However, according to classic solidification theory, the high density of nucleation sites counteracts the large G value, and may lead to the formation of fully equiaxed grain microstructures [44,50–55]. There have been two experimental studies, to the best of our knowledge, demonstrating this counteracting effect [56,57]. One example is the AM-ed Sc- and Zr-modified aluminum alloy prepared by Yang et al. [56]. After careful manipulation of the processing parameters (e.g. lower scan speed and higher platform temperature) and hence the solidification conditions (e.g. lower G value), they additively manufactured nearly equiaxed grain microstructures, thanks to the Al$_3$(Sc,Zr) particles as heterogenous nucleation sites during solidification [56,58]. Another example is shown in the paper by Martin et al. [57]. They decorated aluminum alloy powders with certain nanoparticles, which act as effective heterogenous nucleation sites and hence facilitate the formation of fully equiaxed grain
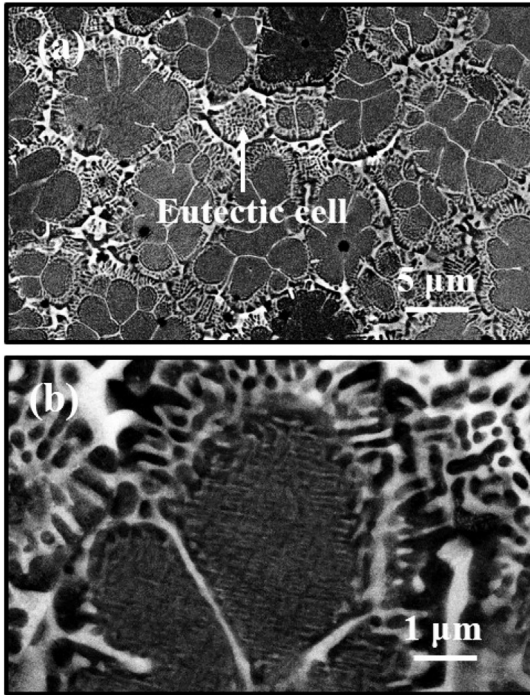
Fig. 5. BSE images of the LENS™-deposited AlCoCrFeNiTi$_{0.5}$ specimen showing microstructural details. (a) Low magnification BSE micrograph, showing equiaxed grains delineated by intergranular bright phases. A eutectic cell at grain boundary is also marked. (b) High magnification BSE image showing eutectic structures clinging to proeutectic dendrites.

microstructures during the AM process. These two experimental studies are very consistent with the classic solidification theory, and both experimental and theoretical studies show that a high density of nucleation sites makes it possible to form fully equiaxed grain microstructures in the AM process, despite a very extreme G value. Further investigations are therefore performed in our study to evaluate the density of nucleation sites in the AlCoCrFeNiTi$_{0.5}$ alloy and probe into their possible origins.

4.2.2. Nucleation
4.2.2.1. Estimation of density of nucleation sites. The density of nucleation sites N_0 can be evaluated by fitting the calculated volume fraction ϕ_{AM} of equiaxed grains in the final AM-ed specimen to the measured one. The calculated volume fraction ϕ_{AM} can be given

by the following equation [53]:

$$\phi_{AM} = 1 - exp\left\{\frac{-4\pi N_0}{3 \cdot \left[\sqrt{nG^n/(Va)\cdot(n+1)}\right]^3}\right\} \tag{1}$$

where a and n are material constants. This equation is valid for G in the order of 10^3 K/mm and V in the order of 10 mm/s. The measured volume fraction $\phi_{AM} = 95.5\%$ of the equiaxed grains in the LENS™-manufactured specimen has been determined by EBSD analysis. Therefore, the density of nucleation sites N_0 is estimated to be a minimum of 3×10^9 /mm^3 (i.e. $N_0 \geq 3 \times 10^9$ /mm^3), assuming $a = 1.25 \times 10^3$ K$^{3.4}$ s/mm and $n = 3.4$, as shown in Fig. 8. In other words, only when the N_0 value reaches or exceeds 3×10^9 /mm^3, fully equiaxed grain microstructures can be achieved. Therefore, 3×10^9 /mm^3 is a very conservative N_0 value. Anyway, this conservatively estimated $N_0 = 3 \times 10^9$ /mm^3 is already very large as compared with those of previously researched alloys, such as the Al alloys (e.g. Al - 3 wt% Cu, $N_0 = 1$ /mm^3 [44]), Cu alloys (e.g. Cu with rare earth microalloying, $N_0 = 5$ /mm^3 [59]), and Ni-based super-alloys (e.g. CMSX-4, $N_0 = 2 \times 10^6$ /mm^3 [53]).

4.2.2.2. Origin of nucleation sites. Fig. 5 (a) shows that the A2 phases frequently isolate the dendritic arms from their primary stalks, and even split individual grains in two, i.e. a dendrite fragmentation phenomenon during solidification. Such fragmented dendrites should be formed in the very last stage of solidification, when only a minor amount of liquid exists. Therefore, these fragments cannot move freely and have to remain close to their primary stalks. Fig. 9 (a), (b), and (c) show the image quality (IQ), kernel average misorientation (KAM), and IPF maps, respectively. In the IPF map, high angle grain boundaries (HAGBs, misorientation >15°) and low angle grain boundaries (LAGBs, 2° < misorientation <15°) are highlighted in black and red, respectively. Fortunately, this examined region contains a split grain and a LAGB is formed inside (i.e. the red line in Fig. 9 (c)). That means the fragments formed at the last stage of solidification merely experience a small degree of rotation and are not responsible for the new grain formation. However, dendrite fragmentation is predicted to be more frequent at the earlier stage of solidification, and fragments are able to move freely within the mushy zone, or even move out of the mushy zone and into the hot liquid. When these fragments flow out of the mushy zone and contact the hot liquid, they start to dissolve or even disappear. However, the fragments that are merely partially dissolved or are still within the mushy zone can be effective
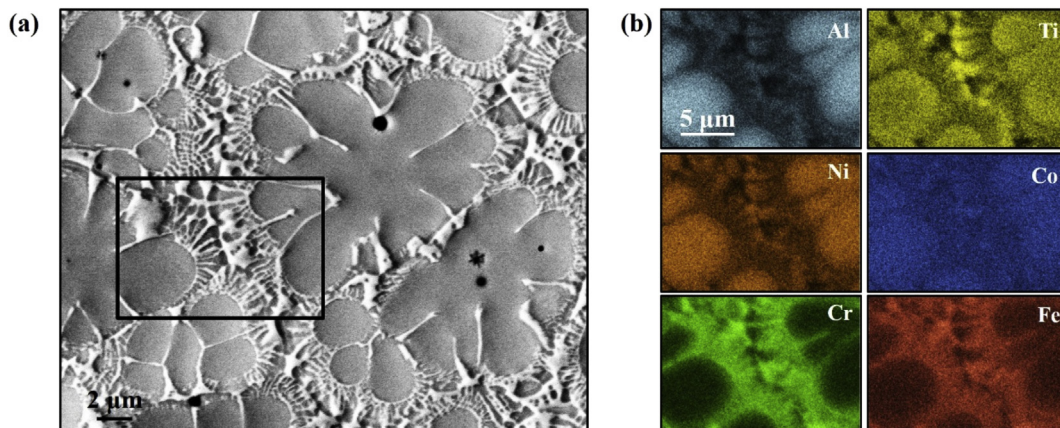

Fig. 6. EDS elemental distribution analysis of the AlCoCrFeNiTi$_{0.5}$ alloy. (a) SE image. (b) EDS elemental distribution of the rectangular region indicated in (a).
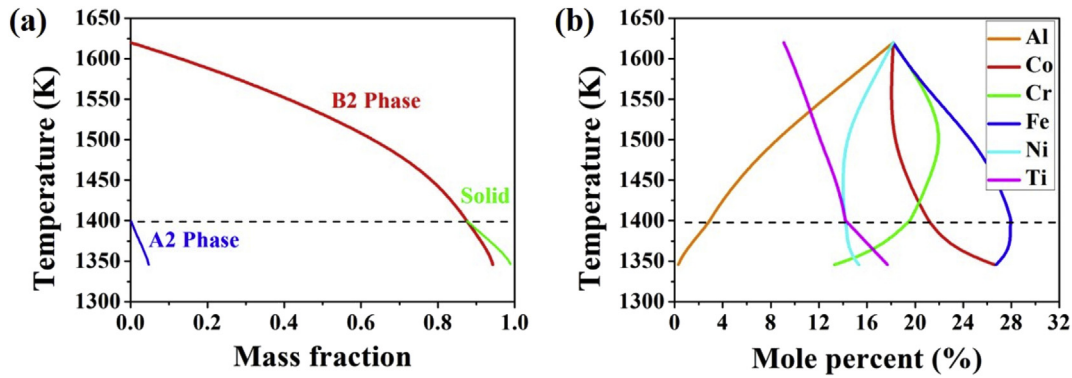
Fig. 7. Scheil's solidification simulation for the AlCoCrFeNiTi$_{0.5}$ alloy. (a) Mass fraction of phases plotted as a function of temperature. Solid refers to B2 plus A2 phases, and above 1400 K, B2- and solid-curves coincide. The solidification mode is L→L + B2→L + B2 + A2. (b) Compositional evolution of the liquid during solidification. The black dashed lines in (a) and (b) indicate the eutectic temperature.

nucleation sites for new grains. According to the results of Scheil's solidification simulation, the solidification range of the experimental AlCoCrFeNiTi$_{0.5}$ alloy is 275 K, which is quite large for fragments to survive. Such freely mobile dendrite fragments are more effective "nucleant agents" as compared with deliberately introduced nucleating agents (e.g. Al$_3$(Sc,Zr) nucleants in aluminum alloys) because dendrite fragments exhibit exactly the same crystal structure and lattice parameter as the solidifying alloys. Furthermore, dendrite fragmentation is a multiplication process, rather than a gradual consumption process, which can produce increasingly more "nucleant agents". More direct observation of dendrite fragmentation and subsequent growth into new grains can be found in the literature dealing with casting and welding processes [60−62]. Overall, we believe that the frequent dendrite fragmentation is the main origin of the large density of nucleation sites of the AlCoCrFeNiTi$_{0.5}$ alloy.

4.2.3. Equiaxed grain microstructure formation: a theoretical analysis

To further understand the formation of the equiaxed grain microstructure, the volume fraction ϕ of the equiaxed crystals at solidification front is estimated for various G - V combinations
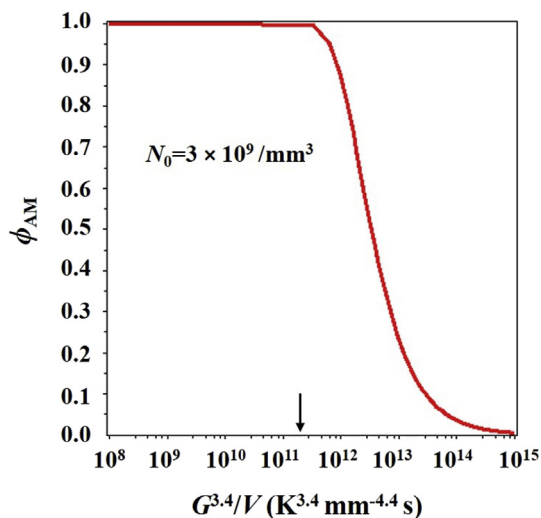

Fig. 8. Determination of the density of nucleation sites N_0 by fitting the calculated volume fraction ϕ_{AM} of equiaxed grains in the final AM-ed specimen to the measured one. The G and V values used are approximately corresponding to the melt pool bottom. The black arrow indicates the maximum $G^{3.4}/V$ value established in this work.

established in this study, with the aid of Gäumann's model [44]. This model considers high velocity effects, and can be used for rapid solidification, e.g. AM processes. The basic physics behind this model is that during columnar dendritic solidification, the solutes pile up in front of the moving solid-liquid interface, assuming a distribution coefficient of <1. Therefore, the local concentration field and the local equilibrium solidification temperature ahead of the solidification interface will be affected. In this case, a constitutionally undercooled region will be established at the dendrite tip, possibly leading to the nucleation and growth of equiaxed crystals. When the volume fraction ϕ of these equiaxed crystals exceeds a critical value (i.e. 49%, as proposed by Hunt [54]), the columnar growth will be prohibited and a fully equiaxed grain microstructure will be achieved.

Assuming the columnar dendrite grows at marginal stability rather than at the extremum used in Hunt's model, the dendritic tip radius R_{tip} can be given by:

$$\frac{\Gamma}{\sigma^* R_{tip}^2} = \sum_{i=1}^{n-1} m_{V,i} \zeta_{C,i} G_{C,i} - G \tag{2}$$

where Γ is the Gibbs-Thomson coefficient, $\sigma^* = 1/(4\pi^2)$ is a stability constant, $m_{V,i}$ is the liquidus slope of component i which is velocity dependent, $\zeta_{C,i}$ is the stability parameter of component i, $G_{C,i}$ is the concentration gradient of component i in the liquid at the dendritic tip. The parameters $m_{V,i}$, $\zeta_{C,i}$, and $G_{C,i}$, are given by following equations:

$$m_{V,i} = m_i \left\{ 1 + \frac{k_i - k_{V,i}[1 - ln(k_{V,i}/k_i)]}{1 - k_i} \right\} \tag{3}$$

$$\zeta_{C,i} = 1 - \frac{2k_{V,i}}{\left[1 + \left(\frac{1}{\sigma^* Pe_i^2}\right)\right]^{1/2} - 1 + 2k_{V,i}} \tag{4}$$

$$G_{C,i} = -\frac{(1 - k_{V,i})V C_{tip,i}}{D_i} \tag{5}$$

where m_i and k_i are the equilibrium liquidus slope and equilibrium partition coefficient of component i, respectively, $k_{V,i}$ is the partition coefficient which is velocity dependent, Pe_i is the solute Péclet number of component i, $C_{tip,i}$ is the concentration of component i in the liquid at the dendrite tip, D_i is the diffusion coefficient of component i in the liquid. The parameters $k_{V,i}$, Pe_i, $C_{tip,i}$, and D_i are given by:
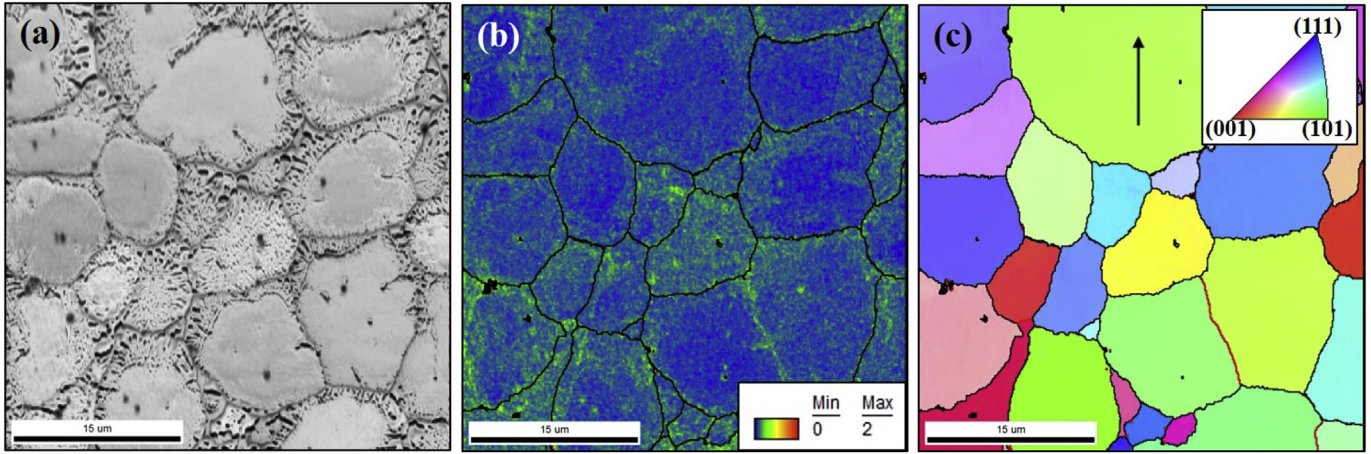
Fig. 9. (a) IQ map. (b) KAM image. (c) IPF map with HAGBs and LAGBs highlighted in black and red, respectively. Note figures (a), (b) and (c) were obtained from the same region of 40 μm by 40 μm.

$$k_{V,i} = \frac{D_i k_i + a_0 V}{D_i + a_0 V} \tag{6}$$

$$Pe_i = \frac{V R_{tip}}{2 D_i} \tag{7}$$

$$C_{tip,i} = \frac{C_{0,i}}{1 - (1 - k_{V,i}) I_v(Pe_i)} \tag{8}$$

$$D_i = D_{0,i} \cdot exp\left(\frac{-Q_i}{R_g T}\right) \tag{9}$$

where a_0 is the characteristic length scale for solute trapping, $C_{0,i}$ is the nominal concentration of component i, $D_{0,i}$ is the diffusion factor of component i, Q_i is the activation energy of component i, $R_g = 8.314 \, J \cdot K^{-1} \cdot mol^{-1}$ is the gas constant, I_v is the Ivantsov function, $I_v(Pe_i) = Pe_i \cdot exp(Pe_i) \cdot E_1(Pe_i)$, and E_1 is the exponential integral function, i.e. $E_1(Pe_i) = \int_{Pe_i}^{\infty} \frac{e^{-t}}{t} dt$. Then the dendrite tip temperature T_{tip} can be calculated by:

$$T_{tip} = T_m + \sum_{i=1}^{n-1} m_{V,i} C_{tip,i} - \frac{2\Gamma}{R_{tip}} - \frac{V}{\mu_k} \tag{10}$$

where T_m is the melting temperature of pure metal, and μ_k is the linear kinetic coefficient. Solving Eqs. (2)–(10), we can achieve the dendrite tip temperature T_{tip}, the concentration of each component in the liquid at the dendrite tip $C_{tip,i}$, and the dendrite tip radius R_{tip} for a given G and V. Then the actual temperature profile in the liquid $T(z)$ can be achieved:

$$T(z) = T_{tip} + G \cdot z \tag{11}$$

where z is the distance from the dendrite tip. Furthermore, the concentration profile of component i in the liquid, $C_i(z)$, and the corresponding liquidus temperature profile, $T_{liquidus}(z)$, are given by:

$$C_i(z) = C_{0,i} + (C_{tip,i} - C_{0,i}) \cdot \frac{E_1\left[Pe_i(2z + R_{tip})/R_{tip}\right]}{E_1(Pe_i)} \tag{12}$$

$$T_{liquidus}(z) = T_L + \sum_{i=1}^{n-1} m_i \left[C_i(z) - C_{0,i}\right] \tag{13}$$

where T_L is the equilibrium liquidus temperature corresponding to the initial composition. The local undercooling profile, $\Delta T(z)$, ahead of the moving solid-liquid interface is therefore given by:

$$\Delta T(z) = T_{liquidus}(z) - T(z) \tag{14}$$

The equiaxed grains may nucleate and grow in this undercooled region, and their volume fraction can be achieved by estimating the maximum radius of an individual equiaxed grain (i.e. the radius of an individual equiaxed grain when the columnar dendrite passes). The size of each equiaxed grain R_e is given by:

$$R_e = \int_0^{z_n} \frac{V_e(z)}{V} dz \tag{15}$$

where z_n is the distance from the solid-liquid interface to the position, where the local undercooling equals the nucleation undercooling, i.e. $\Delta T(z_n) = \Delta T_n$, and $V_e(z)$ is the growth velocity of the equiaxed grains which can be calculated by:

$$V_e(z) = \frac{A \cdot [\Delta T(z)]^2}{\sum_{i=1}^{n-1} C_i(z)} \tag{16}$$

If we assume the dendritic equiaxed grains grow in a spherical mode, the extended volume fraction of the equiaxed grains ϕ_e can be given by:

$$\phi_e = \frac{4\pi R_e^3 N_0}{3} \tag{17}$$

where N_0 is again the density of nucleation sites. Then the actual volume fraction of the equiaxed grains ϕ can be estimated by Avarami equation:

$$\phi = 1 - exp(-\phi_e) \tag{18}$$

The thermophysical parameters associated with this model were largely achieved using Thermo-Calc software equipped with a HEA database, and are shown in Table 1. The ϕ values are calculated

Table 1

Thermophysical parameters associated with Gäumann's model (largely achieved by CALPHAD method on the platform of Thermo-Calc software equipped with a HEA database).

	Al	Co	Cr	Fe	Ti
$C_{0,i}$ (at.%)	18.2	18.2	18.2	18.2	9.1
k_i	1.675	0.964	0.574	0.665	0.554
m_i (K/at.%)	9.740	2.102	-1.495	-1.841	-4.017
$D_{0,i}$ (m²/s)	1.51×10^{-7}	2.30×10^{-7}	2.20×10^{-7}	2.29×10^{-7}	2.08×10^{-7}
Q_i (J/mol)	4.63×10^4	6.54×10^4	6.65×10^4	6.51×10^4	6.08×10^4

to be >49% for various G - V combinations established in this paper, assuming $N_0 = 3 \times 10^9$ /mm³. This indicates that columnar growth will be completed prohibited, by the large amount of equiaxed crystals at the solidification front, and finally a fully equiaxed grain microstructure can be formed, which supports our experimental findings (Fig. 3).

5. Conclusions

The non-equiatomic HEA AlCoCrFeNiTi$_{0.5}$ was additively manufactured by the LENS™ technique in this study. The solidification conditions, grain morphology, phase constitution and microstructural details were investigated, and the underlying mechanisms were explained. The following conclusions can be drawn from our study:

(1) The increase of laser traverse speed or the decrease of laser power leads to a larger temperature gradient. Through the manipulation of the laser traverse speed and laser power, we have established a wide range of temperature gradients (i.e. 85 to 1005 K/mm).

(2) The microstructure of the LENS™-deposited AlCoCrFeNiTi$_{0.5}$ alloy consists of proeutectic B2-structured dendrites delineated by lamellar or rod-like B2/A2 eutectic structures which cling to the proeutectic dendrites. Furthermore, the B2 and A2 phases can nucleate and grow independently at the grain boundaries to form eutectic cells. Such microstructures have been successfully described with the aid of Scheil's solidification model.

(3) Proeutectic B2-structured grains are totally equiaxed and randomly textured. A high density of nucleation sites (a minimum of 3×10^9 /mm³) is estimated, and attributed to frequent dendrite fragmentation. The volume fraction ϕ values of equiaxed crystals at solidification front are estimated to be >49% for various G - V combinations established in this paper. This indicates that fully equiaxed grain microstructures can be formed, and therefore provides a theoretical basis for our experimental findings.

CRediT authorship contribution statement

S. Guan: Conceptualization, Methodology, Data curation, Writing - original draft, Writing - review & editing. **K. Solberg:** Writing - review & editing. **D. Wan:** Writing - review & editing. **F. Berto:** Supervision, Writing - review & editing. **T. Welo:** Supervision, Writing - review & editing. **T.M. Yue:** Supervision, Conceptualization, Writing - review & editing. **K.C. Chan:** Supervision, Conceptualization, Writing - review & editing.

Acknowledgements

References

[1] J.W. Yeh, S.K. Chen, S.J. Lin, J.Y. Gan, T.S. Chin, T.T. Shun, C.H. Tsau, S.Y. Chang, Nanostructured high-entropy alloys with multiple principal elements: novel alloy design concepts and outcomes, Adv. Eng. Mater. 6 (2004) 299−303.

[2] B. Gludovatz, A. Hohenwarter, D. Catoor, E.H. Chang, E.P. George, R.O. Ritchie, A fracture-resistant high-entropy alloy for cryogenic applications, Science 345 (2014) 1153−1158.

[3] B. Gludovatz, A. Hohenwarter, K.V.S. Thurston, H. Bei, Z. Wu, E.P. George, R.O. Ritchie, Exceptional damage-tolerance of a medium-entropy alloy CrCoNi at cryogenic temperatures, Nat. Commun. 7 (2016).

[4] Y. Deng, C.C. Tasan, K.G. Pradeep, H. Springer, A. Kostka, D. Raabe, Design of a twinning-induced plasticity high entropy alloy, Acta Mater. 94 (2015) 124−133.

[5] O.N. Senkov, G.B. Wilks, J.M. Scott, D.B. Miracle, Mechanical properties of Nb$_{25}$Mo$_{25}$Ta$_{25}$W$_{25}$ and V$_{20}$Nb$_{20}$Mo$_{20}$Ta$_{20}$W$_{20}$ refractory high entropy alloys, Intermetallics 19 (2011) 698−706.

[6] A. Takeuchi, K. Amiya, T. Wada, K. Yubuta, W. Zhang, High-entropy alloys with a hexagonal close-packed structure designed by equi-atomic alloy strategy and binary phase diagrams, JOM 66 (2014) 1984−1992.

[7] X.Z. Gao, Y.P. Lu, B. Zhang, N.N. Liang, G.Z. Wu, G. Sha, J.Z. Liu, Y.H. Zhao, Microstructural origins of high strength and high ductility in an AlCoCrFeNi$_{2.1}$ eutectic high-entropy alloy, Acta Mater. 141 (2017) 59−66.

[8] J.Y. He, H. Wang, H.L. Huang, X.D. Xu, M.W. Chen, Y. Wu, X.J. Liu, T.G. Nieh, K. An, Z.P. Lu, A precipitation-hardened high-entropy alloy with outstanding tensile properties, Acta Mater. 102 (2016) 187−196.

[9] Y.-J. Liang, L. Wang, Y. Wen, B. Cheng, Q. Wu, T. Cao, Q. Xiao, Y. Xue, G. Sha, Y. Wang, Y. Ren, X. Li, L. Wang, F. Wang, H. Cai, High-content ductile coherent nanoprecipitates achieve ultrastrong high-entropy alloys, Nat. Commun. 9 (2018) 4063.

[10] Z. Li, K.G. Pradeep, Y. Deng, D. Raabe, C.C. Tasan, Metastable high-entropy dual-phase alloys overcome the strength-ductility trade-off, Nature 534 (2016) 227.

[11] Y.M. Wang, T. Voisin, J.T. McKeown, J.C. Ye, N.P. Calta, Z. Li, Z. Zeng, Y. Zhang, W. Chen, T.T. Roehling, R.T. Ott, M.K. Santala, P.J. Depond, M.J. Matthews, A.V. Hamza, T. Zhu, Additively manufactured hierarchical stainless steels with high strength and ductility, Nat. Mater. 17 (2018) 63.

[12] I. Kunce, M. Polanski, K. Karczewski, T. Plocinski, K.J. Kurzydlowski, Microstructural characterisation of high-entropy alloy AlCoCrFeNi fabricated by laser engineered net shaping, J. Alloys Compd. 648 (2015) 751−758.

[13] T. Fujieda, H. Shiratori, K. Kuwabara, T. Kato, K. Yamanaka, Y. Koizumi, A. Chiba, First demonstration of promising selective electron beam melting method for utilizing high-entropy alloys as engineering materials, Mater. Lett. 159 (2015) 12−15.

[14] H. Shiratori, T. Fujieda, K. Yamanaka, Y. Koizumi, K. Kuwabara, T. Kato, A. Chiba, Relationship between the microstructure and mechanical properties of an equiatomic AlCoCrFeNi high-entropy alloy fabricated by selective electron beam melting, Mater. Sci. Eng. A 656 (2016) 39−46.

[15] J. Joseph, P. Hodgson, T. Jarvis, X.H. Wu, N. Stanford, D.M. Fabijanic, Effect of hot isostatic pressing on the microstructure and mechanical properties of additive manufactured AlxCoCrFeNi high entropy alloys, Mater. Sci. Eng. A 733 (2018) 59−70.

[16] J. Joseph, T. Jarvis, X.H. Wu, N. Stanford, P. Hodgson, D.M. Fabijanic, Comparative study of the microstructures and mechanical properties of direct laser fabricated and arc-melted AlxCoCrFeNi high entropy alloys, Mater. Sci. Eng. A 633 (2015) 184−193.

[17] J. Joseph, N. Stanford, P. Hodgson, D.M. Fabijanic, Tension/compression asymmetry in additive manufactured face centered cubic high entropy alloy, Scr. Mater. 129 (2017) 30−34.

[18] Y. Brif, M. Thomas, I. Todd, The use of high-entropy alloys in additive manufacturing, Scr. Mater. 99 (2015) 93−96.

[19] R. Zhou, Y. Liu, C.S. Zhou, S.Q. Li, W.Q. Wu, M. Song, B. Liu, X.P. Liang, P.K. Liaw, Microstructures and mechanical properties of C-containing FeCoCrNi high-entropy alloy fabricated by selective laser melting, Intermetallics 94 (2018) 165−171.

[20] Z.G. Zhu, Q.B. Nguyen, F.L. Ng, X.H. An, X.Z. Liao, P.K. Liaw, S.M.L. Nai, J. Wei, Hierarchical microstructure and strengthening mechanisms of a CoCrFeNiMn high entropy alloy additively manufactured by selective laser melting, Scr. Mater. 154 (2018) 20−24.

[21] R.D. Li, P.D. Niu, T.C. Yuan, P. Cao, C. Chen, K.C. Zhou, Selective laser melting of an equiatomic CoCrFeMnNi high-entropy alloy: processability, non-equilibrium microstructure and mechanical property, J. Alloys Compd. 746 (2018) 125−134.

[22] A. Piglione, B. Dovgyy, C. Liu, C.M. Gourlay, P.A. Hooper, M.S. Pham, Printability and microstructure of the CoCrFeMnNi high-entropy alloy fabricated by laser powder bed fusion, Mater. Lett. 224 (2018) 22−25.

[23] Z. Qiu, C. Yao, K. Feng, Z. Li, P.K. Chu, Cryogenic deformation mechanism of CrMnFeCoNi high-entropy alloy fabricated by laser additive manufacturing process, Int. J. Lightweight Mater. Manuf. 1 (2018) 33−39.

[24] S. Xiang, H.W. Luan, J. Wu, K.F. Yao, J.F. Li, X. Liu, Y.Z. Tian, W.L. Mao, H. Bai, G.M. Le, Q. Li, Microstructures and mechanical properties of CrMnFeCoNi high entropy alloys fabricated using laser metal deposition technique, J. Alloys Compd. 773 (2019) 387−392.

[25] X. Gao, Y. Lu, Laser 3D printing of CoCrFeMnNi high-entropy alloy, Mater. Lett.

236 (2019) 77−80.

[26] Z. Tong, X. Ren, J. Jiao, W. Zhou, Y. Ren, Y. Ye, E.A. Larson, J. Gu, Laser additive manufacturing of FeCrCoMnNi high-entropy alloy: effect of heat treatment on microstructure, residual stress and mechanical property, J. Alloys Compd. 785 (2019) 1144−1159.

[27] S. Guan, D. Wan, K. Solberg, F. Berto, T. Welo, T.M. Yue, K.C. Chan, Additive manufacturing of fine-grained and dislocation-populated CrMnFeCoNi high entropy alloy by laser engineered net shaping, Mater. Sci. Eng. A 761 (2019), 138056.

[28] Y. Chew, G.J. Bi, Z.G. Zhu, F.L. Ng, F. Weng, S.B. Liu, S.M.L. Nai, B.Y. Lee, Microstructure and enhanced strength of laser aided additive manufactured CoCrFeNiMn high entropy alloy, Mater. Sci. Eng. A 744 (2019) 137−144.

[29] T. Fujieda, H. Shiratori, K. Kuwabara, M. Hirota, T. Kato, K. Yamanaka, Y. Koizumi, A. Chiba, S. Watanabe, CoCrFeNiTi-based high-entropy alloy with superior tensile strength and corrosion resistance achieved by a combination of additive manufacturing using selective electron beam melting and solution treatment, Mater. Lett. 189 (2017) 148−151.

[30] I. Kunce, M. Polanski, J. Bystrzycki, Microstructure and hydrogen storage properties of a TiZrNbMoV high entropy alloy synthesized using laser engineered net shaping (LENS), Int. J. Hydrog. Energy 39 (2014) 9904−9910.

[31] D. Choudhuri, T. Alam, T. Borkar, B. Gwalani, A.S. Mantri, S.G. Srinivasan, M.A. Gibson, R. Banerjee, Formation of a Huesler-like $L2_1$ phase in a CoCrCuFeNiAlTi high-entropy alloy, Scr. Mater. 100 (2015) 36−39.

[32] T. Borkar, V. Chaudhary, B. Gwalani, D. Choudhuri, C.V. Mikler, V. Soni, T. Alam, R. V. Ramanujan, R. Banerjee, A combinatorial approach for assessing the magnetic properties of high entropy alloys: role of Cr in AlCoxCr1−xFeNi, Adv. Eng. Mater. 19 (2017), 1700048.

[33] T. Borkar, B. Gwalani, D. Choudhuri, C.V. Mikler, C.J. Yannetta, X. Chen, R.V. Ramanujan, M.J. Styles, M.A. Gibson, R. Banerjee, A combinatorial assessment of AlxCrCuFeNi2 (0 < x < 1.5) complex concentrated alloys: microstructure, microhardness, and magnetic properties, Acta Mater. 116 (2016) 63−76.

[34] B. Gwalani, V. Soni, O.A. Waseem, S.A. Mantri, R. Banerjee, Laser additive manufacturing of compositionally graded AlCrFeMoVx (x = 0 to 1) high-entropy alloy system, Opt. Laser Technol. 113 (2019) 330−337.

[35] L. Thijs, M.L.M. Sistiaga, R. Wauthle, Q. Xie, J.-P. Kruth, J. Van Humbeeck, Strong morphological and crystallographic texture and resulting yield strength anisotropy in selective laser melted tantalum, Acta Mater. 61 (2013) 4657−4668.

[36] E. Chauvet, P. Kontis, E.A. Jagle, B. Gault, D. Raabe, C. Tassin, J.J. Blandin, R. Dendievel, B. Vayre, S. Abed, G. Martin, Hot cracking mechanism affecting a non-weldable Ni-based superalloy produced by selective electron beam melting, Acta Mater. 142 (2018) 82−94.

[37] G.P. Dinda, A.K. Dasgupta, J. Mazumder, Texture control during laser deposition of nickel-based superalloy, Scr. Mater. 67 (2012) 503−506.

[38] L. Thijs, K. Kempen, J.P. Kruth, J. Van Humbeeck, Fine-structured aluminium products with controllable texture by selective laser melting of pre-alloyed AlSi10Mg powder, Acta Mater. 61 (2013) 1809−1819.

[39] B.E. Carroll, T.A. Palmer, A.M. Beese, Anisotropic tensile behavior of Ti-6Al-4V components fabricated with directed energy deposition additive manufacturing, Acta Mater. 87 (2015) 309−320.

[40] X. Tan, Y. Kok, Y.J. Tan, M. Descoins, D. Mangelinck, S.B. Tor, K.F. Leong, C.K. Chua, Graded microstructure and mechanical properties of additive manufactured Ti-6Al-4V via electron beam melting, Acta Mater. 97 (2015) 1−16.

[41] T. Ishimoto, K. Hagihara, K. Hisamoto, S.H. Sun, T. Nakano, Crystallographic texture control of beta-type Ti-15Mo-5Zr-3Al alloy by selective laser melting for the development of novel implants with a biocompatible low Young's modulus, Scr. Mater. 132 (2017) 34−38.

[42] Y.Y. Zhu, D. Liu, X.J. Tian, H.B. Tang, H.M. Wang, Characterization of

microstructure and mechanical properties of laser melting deposited Ti-6.5Al-3.5Mo-1.5Zr-0.3Si titanium alloy, Mater. Des. 56 (2014) 445−453.

[43] L.L. Parimi, G.A. Ravi, D. Clark, M.M. Attallah, Microstructural and texture development in direct laser fabricated IN718, Mater. Charact. 89 (2014) 102−111.

[44] M. Gäumann, R. Trivedi, W. Kurz, Nucleation ahead of the advancing interface in directional solidification, Mater. Sci. Eng. A 226 (1997) 763−769.

[45] H. Rao, S. Giet, K. Yang, X. Wu, C.H.J. Davies, The influence of processing parameters on aluminium alloy A357 manufactured by selective laser melting, Mater. Des. 109 (2016) 334−346.

[46] Y.J. Zhou, Y. Zhang, Y.L. Wang, G.L. Chen, Solid solution alloys of AlCoCrFeNiTix with excellent room-temperature mechanical properties, Appl. Phys. Lett. 90 (2007), 181904.

[47] Y.J. Zhou, Y. Zhang, T.N. Kim, G.L. Chen, Microstructure characterizations and strengthening mechanism of multi-principal component AlCoCrFeNiTi0.5 solid solution alloy with excellent mechanical properties, Mater. Lett. 62 (2008) 2673−2676.

[48] M. Löbel, T. Lindner, T. Mehner, T. Lampke, Influence of titanium on microstructure, phase formation and wear behaviour of AlCoCrFeNiTix high-entropy alloy, Entropy 20 (2018).

[49] S. Ozbilen, Satellite formation mechanism in gas atomised powders, Powder Metall. 42 (1999) 70−78.

[50] W. Kurz, C. Bezencon, M. Gäumann, Columnar to equiaxed transition in solidification processing, Sci. Technol. Adv. Mat. 2 (2001) 185−191.

[51] M. Gäumann, S. Henry, F. Cleton, J.D. Wagniere, W. Kurz, Epitaxial laser metal forming: analysis of microstructure formation, Mater. Sci. Eng. A 271 (1999) 232−241.

[52] M. Rappaz, W.J. Boettinger, On dendritic solidification of multicomponent alloys with unequal liquid diffusion coefficients, Acta Mater. 47 (1999) 3205−3219.

[53] M. Gäumann, C. Bezencon, P. Canalis, W. Kurz, Single-crystal laser deposition of superalloys: processing-microstructure maps, Acta Mater. 49 (2001) 1051−1062.

[54] J.D. Hunt, Steady-state columnar and equiaxed growth of dendrites and eutectic, Mater. Sci. Engng. 65 (1984) 75−83.

[55] W. Kurz, B. Giovanola, R. Trivedi, Theory of microstructural development during rapid solidification, Acta Metall. 34 (1986) 823−830.

[56] K.V. Yang, Y.J. Shi, F. Palm, X.H. Wu, P. Rometsch, Columnar to equiaxed transition in Al-Mg(-Sc)-Zr alloys produced by selective laser melting, Scr. Mater. 145 (2018) 113−117.

[57] J.H. Martin, B.D. Yahata, J.M. Hundley, J.A. Mayer, T.A. Schaedler, T.M. Pollock, 3D printing of high-strength aluminium alloys, Nature 549 (2017) 365−369.

[58] A.B. Spierings, K. Dawson, T. Heeling, P.J. Uggowitzer, R. Schäublin, F. Palm, K. Wegener, Microstructural features of Sc- and Zr-modified Al-Mg alloys processed by selective laser melting, Mater. Des. 115 (2017) 52−63.

[59] Y. Chen, S. Zhang, H. Song, M. Cheng, H. Li, J. Liu, Sudden transition from columnar to equiaxed grain of cast copper induced by rare earth microalloying, Mater. Des. 91 (2016) 314−320.

[60] G. Zimmermann, C. Pickmann, M. Hamacher, E. Schaberger-Zimmermann, H. Neumann-Heyme, K. Eckert, S. Eckert, Fragmentation-driven grain refinement in directional solidification of AlCu10wt-% alloy at low pulling speeds, Acta Mater. 126 (2017) 236−250.

[61] H. Yasuda, Y. Yamamoto, N. Nakatsuka, M. Yoshiya, T. Nagira, A. Sugiyama, I. Ohnaka, K. Uesugi, K. Umetani, In situ observation of solidification phenomena in Al-Cu and Fe-Si-Al alloys, Int. J. Cast Met. Res. 22 (2009) 15−21.

[62] H. Yasuda, Y. Yamamoto, N. Nakatsuka, T. Nagira, M. Yoshiya, A. Sugiyama, I. Ohnaka, K. Umetani, K. Uesugi, In situ observation of nucleation, fragmentation and microstructure evolution in Sn-Bi and Al-Cu alloys, Int. J. Cast Met. Res. 21 (2008) 125−128.